

Research on the Anti-tumor Activity of Novel Histone Deacetylase Inhibitors based on 3D QSAR Model

Liqliang Meng¹, Yanhong Ou-Yang¹, Jianxin Yao¹, Fuyin Lv¹ and Yuehong Huo^{2*}

¹Department of Pharmacy, The Fifth People's Hospital of Datong City, Datong Shanxi Province, People's republic of china

*Corresponding Author

Yuehong Huo, The Fifth People's Hospital of Datong City, Datong Shanxi Province, People's Republic of China.

²Department of Rheumatology, The Fifth People's Hospital of Datong City, Datong Shanxi Province, People's republic of china

Submitted: 2023, Nov 01 ; Accepted: 2023, Dec 05; Published: 2023, Dec 15

Citation: Meng, L., Yang, Y. O., Yao, J., Lv, F., Huo, Y. (2023). Research on the Anti-tumor Activity of Novel Histone Deacetylase Inhibitors based on 3D QSAR Model. *Int J Cancer Res Ther*, 8(4), 186-201.

Abstract

Background: Histone deacetylases (HDACs) pertain to the category of Zn^{2+} or nicotinamide adenine dinucleotide (NAD⁺)-dependent proteolytic enzymes. While the antitumor effect of HDAC inhibitors alone has been demonstrated and the effect of HDAC inhibitors on solid tumors is not ideal, which considerably limits their clinical use. Therefore, the search for novel HDAC inhibitors equipped with specific inhibitors is extremely urgent and necessary.

Methods: 3D-QSAR was employed to investigate insights into the crucial structural element that effect the activity of novel HDAC small molecule inhibitors. The best saliency CoMFA and CoMSIA models are obtained using 55 molecules in the training set and 16 molecules in the test set.

Results: The statistical quality of the generated model is demonstrated by internal and external cross-validations. The CoMFA model obtained satisfactory values ($q^2 = 0.664$, $r^2 = 0.917$, $SEE = 0.217$) while optimized CoMSIA model exceed with ($q^2 = 0.672$, $r^2 = 0.948$, $SEE = 0.175$).

Conclusion: The statistical parameters from 3D-QSAR models reveal that the results are reliable and significant with strong predictive ability. These theoretical results may contribute to the design of novel HDAC small molecule inhibitors with enhanced activity for the treatment of cancer.

Keywords: 3D-QSAR, CoMFA, CoMSIA, PLS, HDAC, Small Molecule Inhibitors

1. Introduction

It must be admitted that cancer is a widespread disease with a high mortality rate. Other than genetic factors, the development of cancer touches upon epigenetic modifications, including covalent modifications of DNA (methylation and demethylation) and histones [1]. The post-translational modification of histones will form the so-called "histone code", which provides a recognition marker that regulates gene transcription by inducing the synergistic or antagonistic effect on the binding of additional proteins to DNA [2,3]. Histone deacetylases (HDACs) pertain to the category of Zn^{2+} or nicotinamide adenine dinucleotide (NAD⁺)-dependent proteolytic enzymes, which could dislodge acetyl groups from the ϵ -amino group of lysine residues located at the N-terminus of core histones [4,5]. On account of the deacetylation property, HDACs partake in the regulation and modulation of a large amount of momentous biological signaling pathways, including cell

differentiation, proliferation, angiogenesis and apoptosis [6]. Up to the present, a total of 18 HDAC isozymes have been identified in humans. HDACs are classified into 4 disparate classes on the grounds of their structural, number of catalytically active sites and the sequence homology to the yeast original enzymes [7]. Among the rest, classes I (1, 2, 3, 8), II (4, 5, 6, 7, 9, 10) and IV (11) HDACs belong to Zn^{2+} -dependent metalloenzymes, while class III (SIRT1-7) are NAD⁺-dependent HDACs [8].

Meanwhile, HDACs attract more and more attention from the academia and pharmaceutical industry [9]. There is plenty of evidence that HDACs overexpression has been discovered in all sorts of human cancers, including myeloma, gastric, pancreatic, colorectal and prostate cancers [10]. With the gradual elucidation of the relationship between HDACs and tumors, it has been widely recognized that HDACs have emerged as extremely attractive

targets for the discovery of anticancer agents. Regrettably, only a smattering of promising HDAC enzyme inhibitors, which block the cancer-preventing process, have been tested and evaluated in various stages of clinical trials during the lengthy discovery process. Until now, only five HDAC inhibitors namely, Vorinostat (SAHA), Romidepsin (FK228), Belinostat (PXD101), Panobinostat (LBH589) and Pracinostat (SB939) were resoundingly authorized by the United States Food and Drug Administration and one HDAC inhibitor namely Chidamide (CS055) obtained the approval from the China Food and Drug Administration [11,12]. Both of them are approved for the treatment of cutaneous T-cell lymphoma, peripheral T-cell lymphoma or multiple myeloma [13]. Although HDAC inhibitors reveal potent antitumor effects, most broad-spectrum HDAC inhibitors may cause severe side effects of which the most common symptoms were thrombocytopenia, neutropenia, anemia, fatigue, and diarrhea [14]. Therefore, the development of novel and efficient HDAC inhibitors with high selectivity and low toxicity has the potential to profoundly tap their clinical potential in cancer therapy [15].

Three-dimensional quantitative structure activity relationship (3D-QSAR) is one of the computational methods for drug design based on ligands and plays a crucial role in computer-aided drug design [16]. At the same time, quantitative relationships between a sequence of compounds and the associated biological activity have been explored using theoretical calculations and statistical analysis tools, providing some useful clues to the structural modifications of the compounds. On account of the high-precision features of the

Comparative Molecular Field Method (CoMFA) and Comparative Molecular Similarity Analysis (CoMSIA) models, they have emerged as the most resultful 3D-QSAR tools based on statistical techniques [17]. In CoMFA, biological activity is related to steric and electrostatic parameters. Whereas the advantage of CoMSIA is its takes into account five different property fields: hydrophobic, hydrogen bond donor (HBD), hydrogen bond acceptor (HBA), steric field and electrostatic parameters [18]. The purpose of this research work is to produce a model with high predictive power, to provide more informed directions for further structural modifications, and to guide the design of novel high-potency HDAC inhibitors with specific inhibitory effects.

2. Materials and Methods

2.1. 3D-QSAR Dataset

In the present QSAR research, a total of 71 HDAC inhibitors and related bioactivities were gathered from the work reported in the literature [19]. The experimental IC_{50} values were converted into pIC_{50} ($-\log IC_{50}$) values as dependent variable and QSAR descriptors of CoMFA and CoMSIA were expressed as independent variables in 3D-QSAR analysis [20]. The chemical structures and corresponding biological data of all compounds are presented in Table 1. The range of pIC_{50} was found to be 4.73-8.28 (Fig. 1). The extensive dataset covered pIC_{50} values of 3 log units were randomly chosen as the training set (55 molecules, 77%) to generate the 3D-QSAR models and assess predictive ability of the obtained models with the test set (16 molecules, 23%).

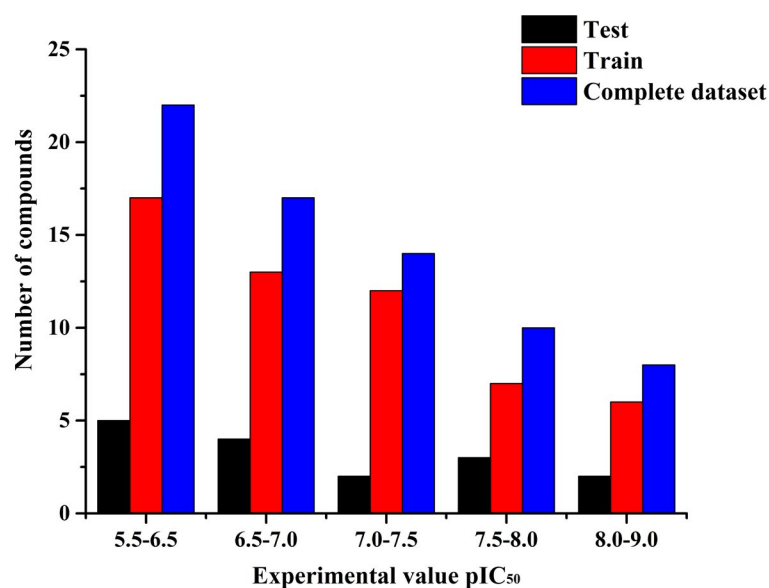
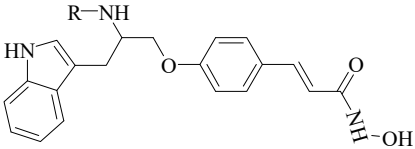
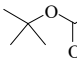
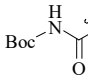
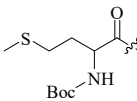
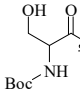
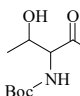
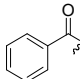
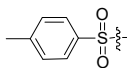
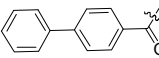
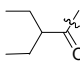
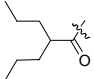
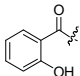
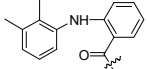
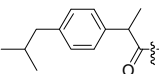
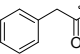
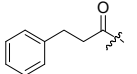
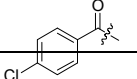
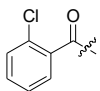
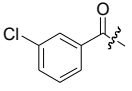
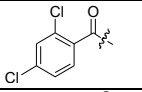
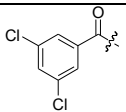
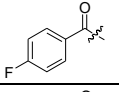
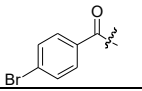
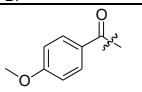
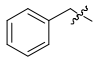
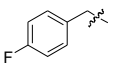
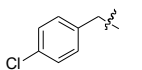
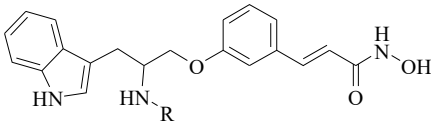
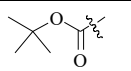
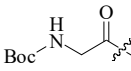
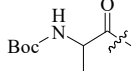
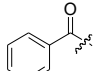
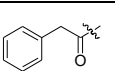
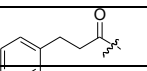
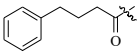
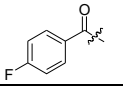
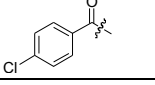
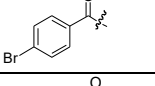
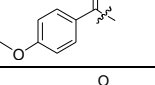
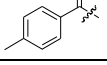
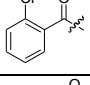
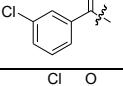
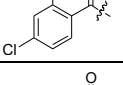
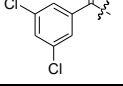
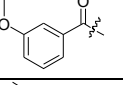
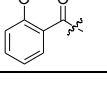
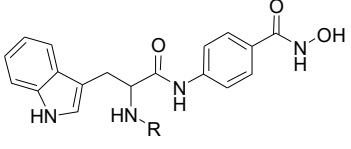
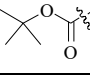
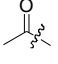
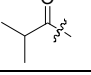
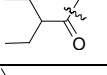
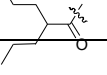
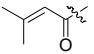
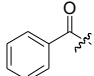
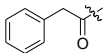
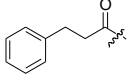
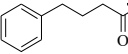
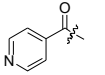
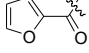
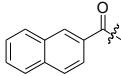
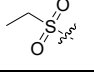
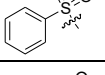
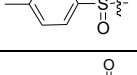
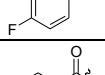
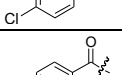
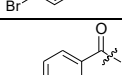
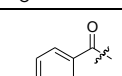
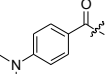
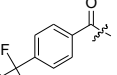
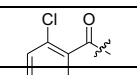



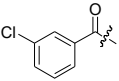
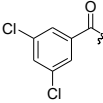
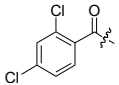
Figure 1: Distribution of experimental inhibitory activities (pIC_{50}) for the training and test sets compounds in the QSAR models.

			
Compound	R	IC ₅₀ (nM)	pIC ₅₀
10a		530.0	6.28
11a		96.6	7.02
11b		255.1	6.59
11c		97.6	7.01
11d		84.3	7.07
*11e		10.5	7.98
11f		636.9	6.20
*11g		1703.4	5.77
*11i		130.3	6.89
11j		977.8	6.01
11k		20.8	7.68
*11l		673.7	6.17
11m		1043.1	5.98
*11p		23.2	7.63
11q		52.3	7.28
11r		5.6	8.25

11s		50.4	7.30
11t		147.9	6.83
*11u		186.5	6.73
11v		209.8	6.68
11w		6.7	8.17
11x		20.4	7.69
*11y		4.8	8.32
*24a		198.5	6.70
24b		148.0	6.83
*24c		157.8	6.80
			
29a		917.4	6.04
29b		886.4	6.05
29c		861.5	6.06
29d		421.4	6.38
29e		447.7	6.35
29f		464.5	6.33

29g		498.6	6.30
29h		447.6	6.35
29i		369.8	6.43
29j		692.4	6.16
29k		191.2	6.72
29l		218.7	6.66
29m		81.9	7.09
29n		357.9	6.45
29o		258.9	6.59
29p		779.0	6.11
*29q		67.4	7.17
*29r		38.5	7.41
			
36a		280.4	6.55
*36b		425.0	6.37
*36c		526.4	6.28
*36d		332.8	6.48
36e		211.5	6.67

36f		138.8	6.86
36g		23.8	7.62
36h		47.5	7.32
36i		59.7	7.22
36j		98.7	7.01
36k		100.1	7.00
36l		31.0	7.51
*36m		27.0	7.57
36n		1085.8	5.96
36o		177.8	6.75
36p		195.7	6.71
*36q		2.4	8.62
36r		1.5	8.82
36s		3.7	8.43
36t		8.6	8.07
36u		13.0	7.89
36v		4.7	8.33
36w		30.0	7.52
36x		156.8	6.80

36y		43.1	7.37
36z		41.2	7.39
37a		23.3	7.63

* Test sets

Table 1: Structures and Bioactivities of the Training and Test Sets of Molecule.

2.2. Molecular Modeling and Alignment

All the entire molecular modeling and statistical analysis of CoMFA and CoMSIA were performed by means of SYBYL-X2.0 package (Tripos, Inc, St. Louis, MO, USA) [21]. Energy minimization was performed using the Tripos Force Field with a distance-dependent dielectric function and the Powell conjugate gradient algorithm with a convergence criterion of 0.005 kcal/(Å mol) and the maximum iteration setting as 1000 [22]. The partial atomic charges of each compound structure was calculated by the Gasteiger-Huckel method, whereas additional factors were fixed as default [23].

During the generation of 3D-QSAR models, the molecular alignments of the compounds was considered as the most crucial step for the robustness and predictive power of CoMFA and CoMSIA models [24]. The most potent compound of the dataset, 36r, was chosen as the template on which all molecules of the training set were aligned according to the largest common substructure. The compound 36r, marked in red by the common substructure, and the final superposition of the compounds are shown in Figs. (2 and 3), respectively.

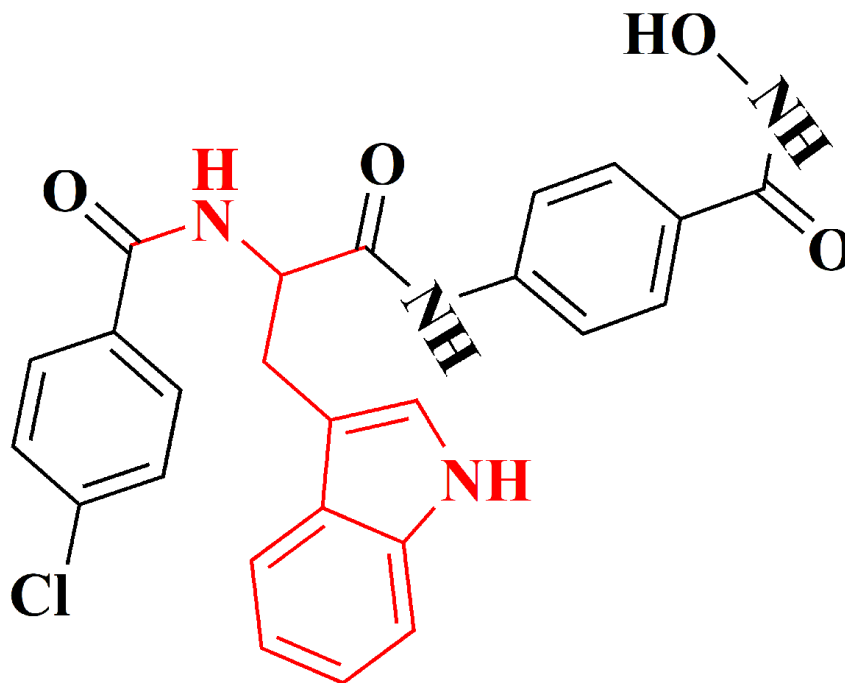


Figure 2: Structure of compound 36r regarded as template compound in 3D-QSAR modeling. The compound alignments of common substructure is represented in red.

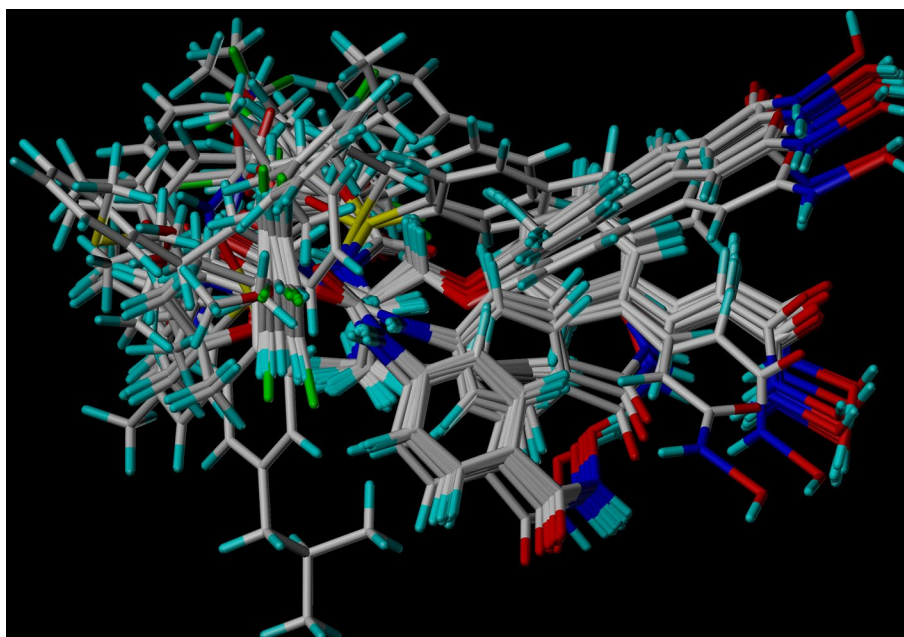


Figure 3: Alignment of 55 compounds of training set for 3D-QSAR studies.

2.3. CoMFA and CoMSIA Analyses

Both of the CoMFA and CoMSIA models were established based on the structural alignments of series. After each alignment, the CoMFA and CoMSIA descriptors of different force fields were placed in a common rectangular grid with a grid spacing of 2.0 Å using sp^3 -hybridised carbon atom with +1.0 charge served as a probe atom [25].

For the CoMFA analysis, the steric and electrostatic fields energy were estimated based on the principle of Lennard-Jones and Coulomb functions [26]. The energy cutoff was fixed at 30 kcal/mol for both fields. To reduce noise and speed up the calculation of potentials, column filtering was tested in the range of 0.0 to 2.0 kcal/mol and a threshold column filtering value of 2.0 kcal/mol [25]. The “StDev*Coefficients” values as various weighting factors were performed in addition to grid spacing for getting the better models, which can increase the resolution and predictability (q^2 , cross-validated r^2) related to the following PLS analysis.

As in the CoMSIA analysis, the calculations were performed using the same grid-box similarity index descriptors as used in the CoMFA calculations. Five physicochemical properties of steric, electrostatic, hydrophobic, hydrogen bonding donor and acceptor fields were calculated at each lattice point of the grid box consisting of a probe atom with a radius of 1 Å for all five fields with +1 charge [26]. In addition, the Gaussian function is distinguished in the CoMSIA analysis by the distance dependence between the molecular atom and the probe atom, hence no cut-off

value is required [27].

2.4. Partial Least Square (PLS) Analysis

Partial least squares analysis (PLS) statistical as an extension of multiple regression analysis was applied to derive 3D-QSAR models [28]. PLS regression analysis was introduced to construct a linear correlation between the dependent variable (pIC_{50} values) and the independent variable (CoMFA/CoMSIA energy fields) of the dataset.

In order to better determine the predictive capability of the 3D-QSAR models, the cross-validated correlation coefficient (q^2) and optimum number of components (ONC) were calculated by the leave-one-out (LOO) method for the optimization of the CoMFA and CoMSIA model [29]. For further internal validation of the models, the non-cross-validated correlation coefficient (r^2), F-statistic (F) value, standard error of estimate (SEE) and contributions of each model field were determined by using non-cross-validated analysis.

3. Results and Discussion

3.1. CoMFA and CoMSIA Statistical Results

The statistical parameters obtained for the CoMFA and CoMSIA analyses which presented in Table 2 were performed on the basis of a 55 molecules training set. These statistics parameters indicate the obtained CoMFA and CoMSIA models represented the satisfactory internal predictive capability ($q^2 > 0.5$) as well as robustness ($r^2 > 0.8$).

Parameters	CoMFA	CoMSIA
q^2 ^a	0.664	0.672
r^2 ^b	0.917	0.948
N ^c	6	8
F ^d	100.436	104.543
SEE ^e	0.217	0.175
Steric	0.417	-
Electrostatic	0.583	0.212
Hydrophobic	-	0.389
H-bond donor	-	0.399
H-bond acceptor	-	-

^a Cross-validated correlation coefficient.
^b Non-cross-validated correlation coefficient.
^c Optimal number of components
^d F-test value.
^e Standard error of estimate.

Table 2: Statistical Parameters of CoMFA and CoMSIA Models by PLS Analysis

Based on the statistical significance of the data, the result of CoMFA model revealed that it was a cross-validated correlation coefficient (q^2) of 0.664 with an optimum number of components of 6. The non-cross-validated PLS assessment resulted in a high non-cross-validated correlation coefficient (r^2) of 0.917 with a low standard error estimate (SEE) of 0.217 and F value of 100.436. The contributions of the steric and electrostatic field descriptors in the CoMFA model are proportional to 0.417 and 0.583, respectively.

In terms of CoMSIA, the model comprised steric (S), electrostatic (E), hydrophobic (H), hydrogen bond donor (D) and acceptor (A) fields. The optimal CoMSIA model was exhibited by the combined EHD model because it possessed the highest cross-validated q^2 value of 0.672 with an optimized component of 8 among the diverse 25 permutations and combinations of all CoMSIA properties (Fig. 4). The non-cross-validated r^2 was found 0.948 with F value of 104.543 and SEE of 0.175. Regarding the CoMSIA model, the contributions from the electrostatic, hydrophobic and hydrogen H-bond donor fields are 0.212, 0.389 and 0.399, respectively.

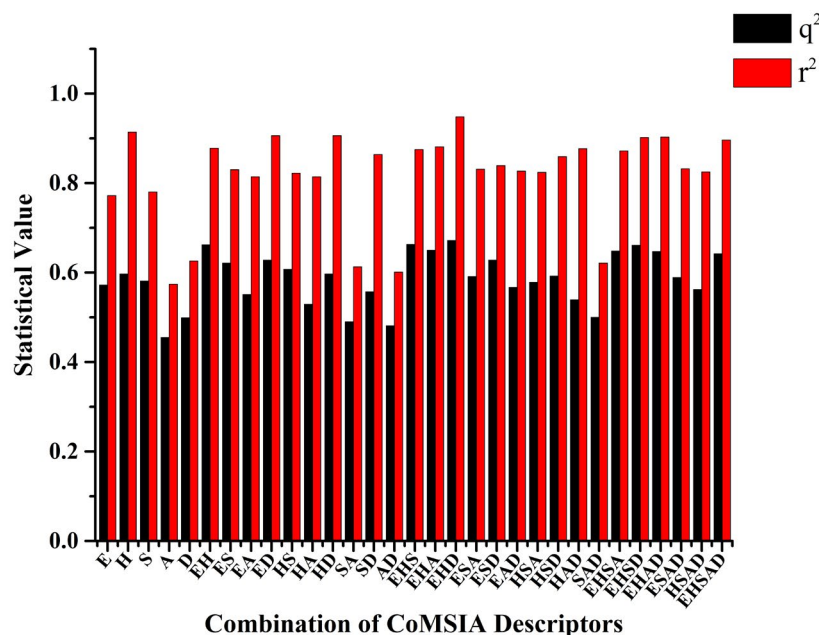


Figure 4: Statistical comparison of 31 different combinations of descriptors for the CoMSIA model.

3.2. Validation of Models

To further ensure the external predictive power, the predictive power of the QSAR model for the external test set of 16 molecules was computationally analyzed. The residuals of the CoMFA and CoMSIA models with experimental activity pIC_{50} values and

predicted activity pIC_{50} values of all set compounds are represented in Figs. (5a and 5b). The correlations between the calculated and actual pIC_{50} values of the whole data set for the CoMFA and CoMSIA model were exhibited in Figs. (6a and 6b). These data confirm the satisfactory predictive capability of the model.

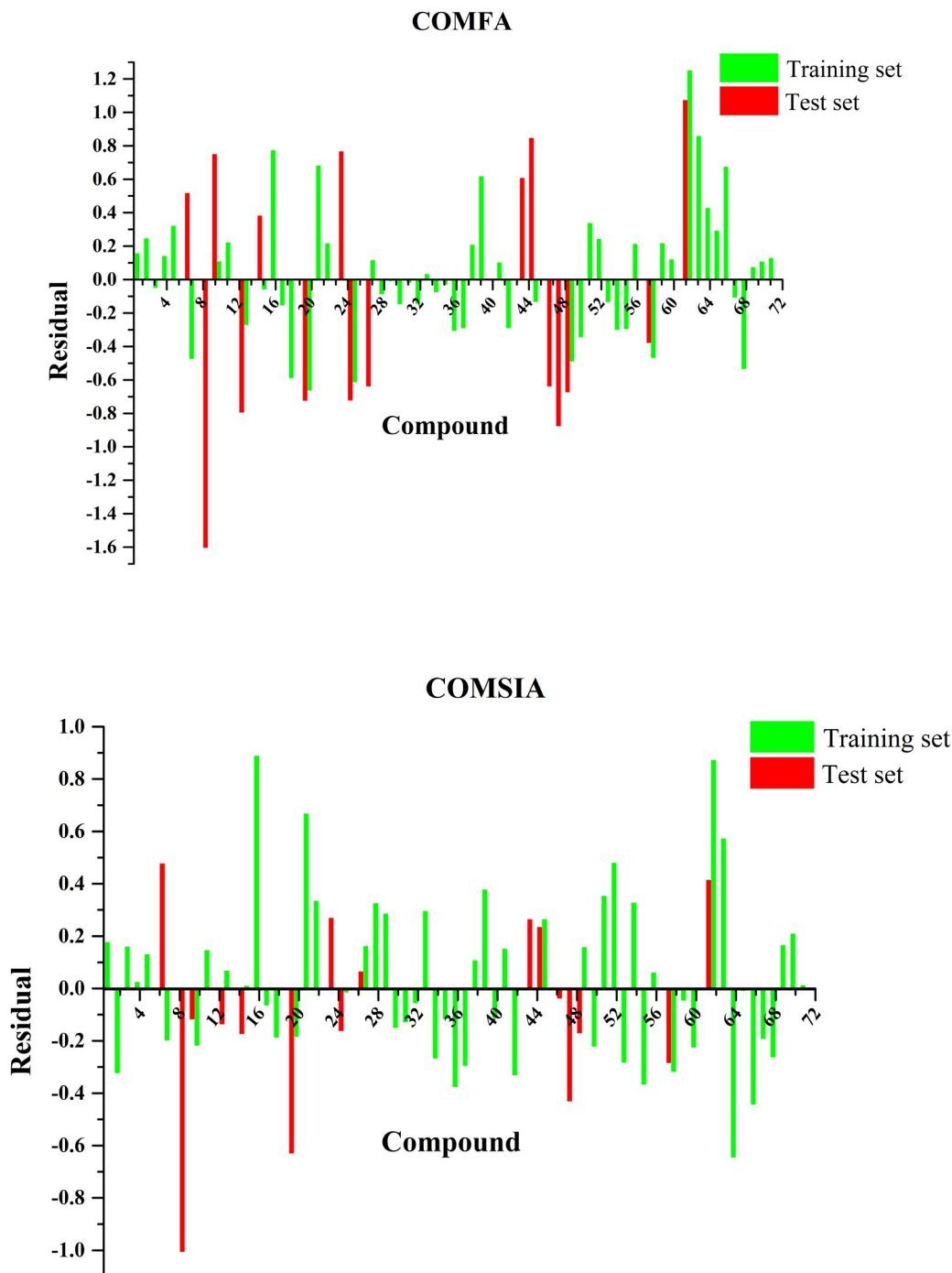


Figure 5: The CoMFA (a) and CoMSIA (b) models of residuals with experimental activities pIC_{50} and predicted activities pIC_{50} of all set compounds.

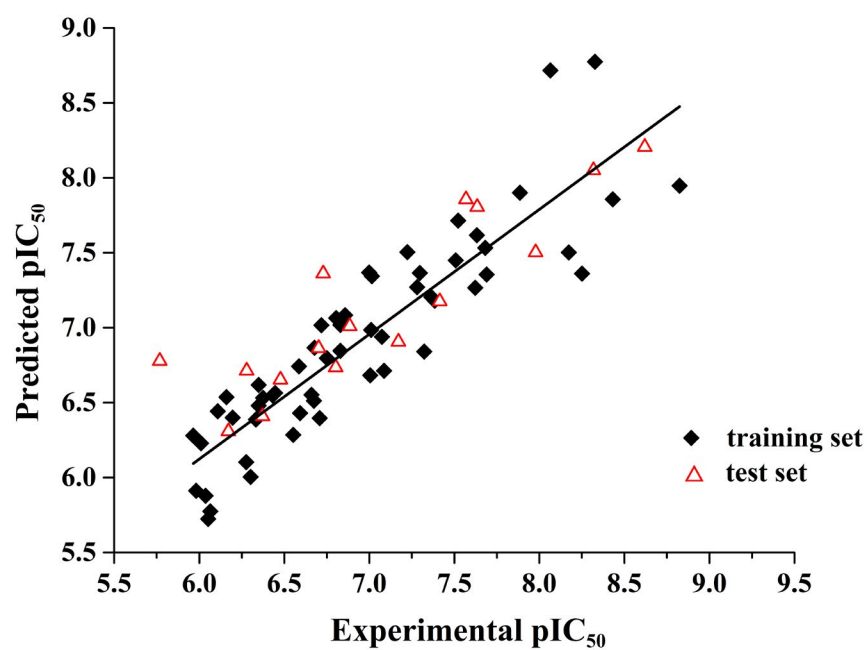
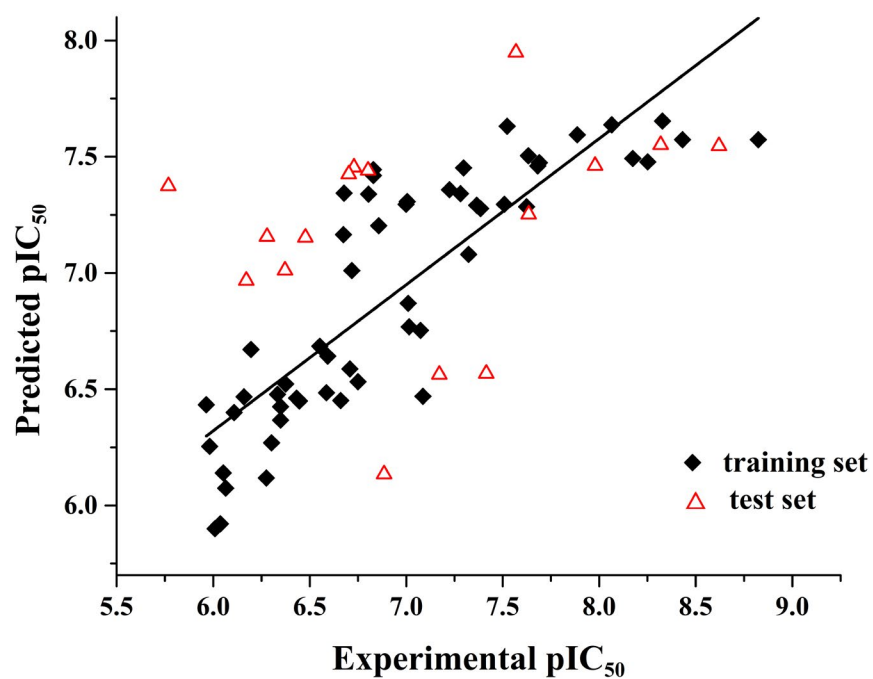


Figure 6: Plots of the experimental pIC_{50} versus predicted pIC_{50} for CoMFA (a) and CoMSIA (b).

3.3. Contour Map Analysis

The 3D-QSAR contour maps of the CoMFA/CoMSIA models are intuitive tools to visualize the impacts of the various fields on the favorable and unfavorable regions of the molecules for biological activity. Meanwhile, the CoMFA and CoMSIA contour plots are also able to identify molecular fragments, functional groups and physicochemical properties that are closely related to the activity of the series. The CoMFA and CoMSIA results were demonstrated by field contribution maps using the standard deviation (StDev) at each grid point and the coefficient from the PLS analysis ($\text{StDev} \times \text{Coefficients}$). For all of the contour maps, the positive and negative areas for each field are shown with a contribution of 80% and 20%, respectively.

3.4. CoMFA Contour Map Analysis

In the case of the CoMFA contour model, in order to visualize the information content of the derived QSAR model, the coefficients from the CoMFA model are plotted to generate the steric and electrostatic contour maps. The results indicate that the proportion of steric field contribution is 41.7%, while the electrostatic field accounts for 58.3% in the fractions of contribution of each field. The CoMFA contour maps related to the steric and electrostatic fields are revealed in Figs. (7a and 7b), along with the most effective HDAC inhibitors (compound 36r) as the template molecule.

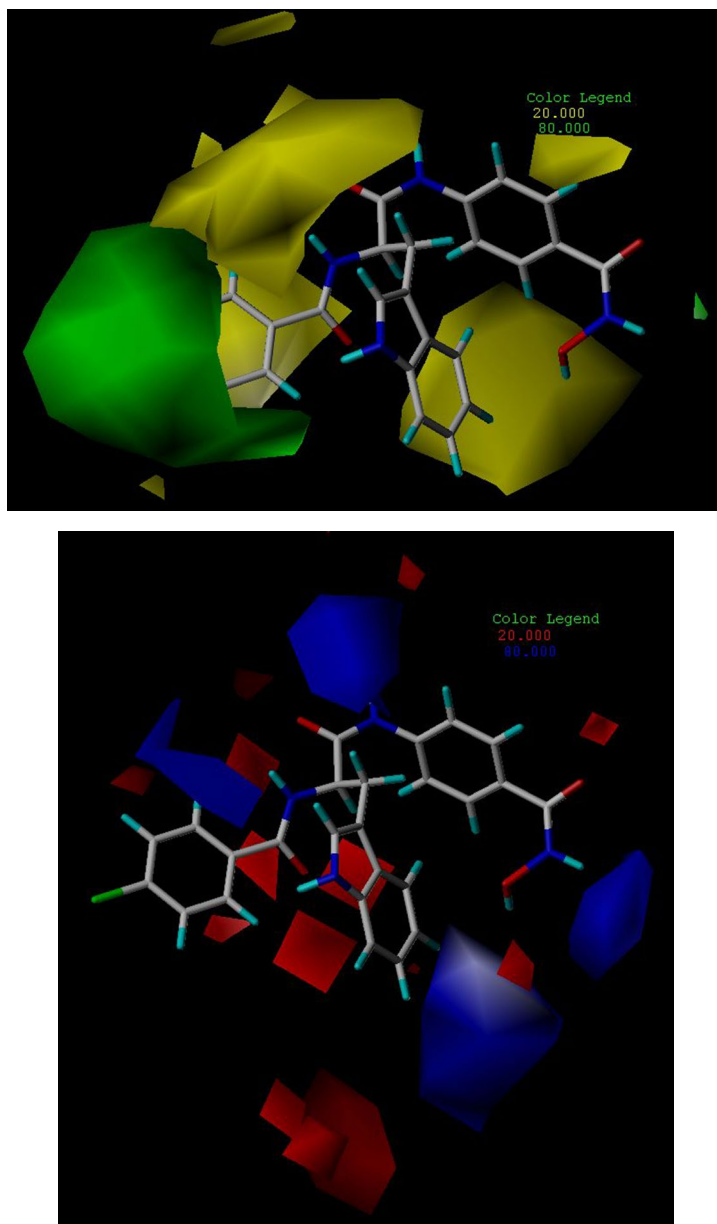


Figure 7: CoMFA $\text{stdev} \times \text{coeff}$ contour plots for steric (a) and electrostatic (b) fields. Compound 36r was displayed as reference. Sterically favored/disfavored areas are shown in green/yellow, while the blue/red polyhedra depict the favorable site for positively/negatively charged groups. Favored and disfavored levels of these displayed interaction fields were fixed at 80% and 20%, respectively.

In CoMFA steric map, Fig. (7a) represents favorable groups (80% contribution) in green color and unfavorable ones (20% contribution) in yellow. The green block indicates a bulky group preference region, while the yellow block indicates that a minor substitution is preferred to enhance activity. This relationship explains that terminal positions in a sequence of compounds are responsible for biological activity. It can be seen that there is a large green contour around the position near the end of the R substitution, which indicates that a large number of substitutions in this region is beneficial for the enhancement of inhibition. This evidence is extremely valuable as a guide for our future chemical structural modifications. For instance, compound 11y ($pIC_{50} = 8.32$) bearing a -OMe group at the 4-position of the benzene ring indicated increased potential activity than compound 11e ($pIC_{50} = 7.98$). The similar phenomenon was observed that the comparison among compounds 36v, 36t and 36g turns out that 36v ($pIC_{50} = 8.33$) > 36t ($pIC_{50} = 8.07$) > 36g ($pIC_{50} = 7.62$) which contains groups -N(CH₃)₂, -OMe and -H, respectively.

As shown in the electrostatic contour maps (Fig. 7b), the preferred regions of the electron-donating group and the electron-withdrawing group are represented by blue and red outlines, where the red contour indicates enhanced biological activity with increasing negative charge, the blue contour indicates

enhanced biological activity with increasing positive charge. The red contours around the position of the group attachment to the nitrogen, illuminate that the electron withdrawing group in this region is favorable for biological activity. This could be due to the higher activity of compound 11w ($pIC_{50} = 8.17$) compared to 24b ($pIC_{50} = 6.83$). At the same time, this is consistent with the fact that the compounds 36r ($pIC_{50} = 8.82$), 36q ($pIC_{50} = 8.62$) and 36s ($pIC_{50} = 8.43$).

3.5. CoMSIA Contour Maps Analysis

The contour maps of all CoMSIA fields (steric and electrostatic, hydrophobic, hydrogen bonding (H-bond) donor and acceptor) that contributed to biological activity are revealed in Fig. 8. In CoMSIA model the contribution for the electrostatic field (21.2%) loses importance compared with CoMFA contour maps. The contributions from the hydrophobic and hydrogen-bond donor fields are 38.9% and 39.9%, respectively.

As shown in Figs. (8a and b), the results of CoMSIA electrostatic and steric contour maps are virtually similar to CoMFA electrostatic and steric fields. But there are still some differences between the steric fields. Even then, the discussion or analysis of these two contour maps will be identical to the analysis of the CoMFA contour map.

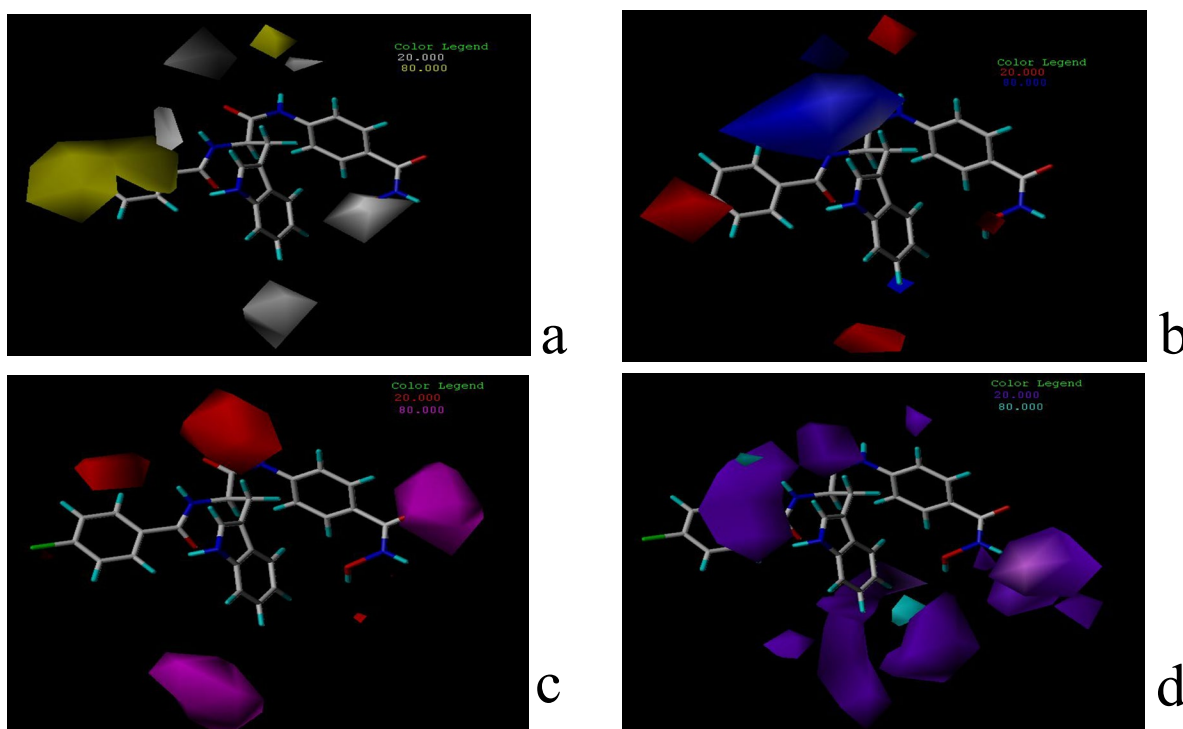


Figure 8: CoMSIA StDev*Coeff contour plots with the combination of compound 36r. (a) Steric contour maps: Green contours indicate regions where bulky groups increase activity; yellow contours indicate regions where bulky groups decrease activity; (b) Electrostatic contour maps: Blue contours indicate regions where positive charges increase activity; red contours indicate regions where negative charges increase activity; (c) Hydrophobic contour maps: yellow contours indicate regions where hydrophobic substituents enhance activity; white contours indicate regions where hydrophobic groups decrease activity; (d) Hydrogen bond donor contour maps: Cyan contours indicate regions where H-bond donor groups increase activity and purple contours indicate the unfavorable regions for hydrogen bond donor substituents;

In the following, we mainly discuss and analyze the hydrophobic and hydrogen bond acceptor fields with large contribution rates. The yellow and gray contours represent hydrophobic and hydrophilic groups, respectively, as shown in Fig. (8c). The white and yellow contour maps highlight regions that are both hydrophilic and hydrophobic in preference. It can be seen that there is a large

yellow contour around the benzene ring, indicating that a large hydrophobic substitution at this position is favorable for enhanced affinity. This is a possible reason why compounds 36v ($pIC_{50} = 8.33$) and 36u ($pIC_{50} = 7.89$) reveal better potency compared to compound 36g ($pIC_{50} = 7.62$) due to increased hydrophobicity.

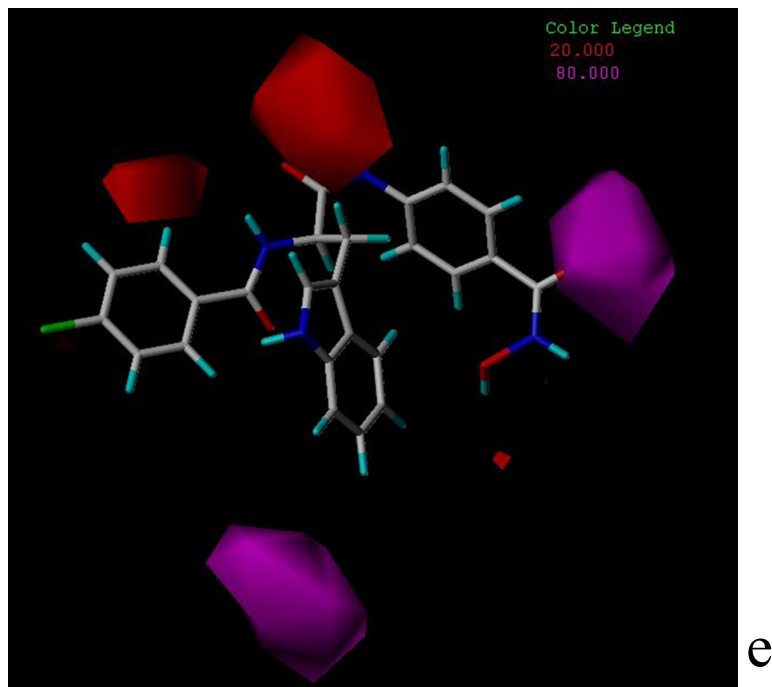


Figure 8: (e) H-bond acceptor contour maps: Magenta contours indicate regions where an H-bond acceptor substituents increase activity; red contours indicate the disfavor regions for H-bond acceptor groups.

The contour map of the CoMSIA H-bond acceptor is connected to the hydrogen bond interaction between the ligand and the target. The contour map of the hydrogen bond acceptor (HBA) is shown in Fig. (8e), the magenta and red contour maps indicate favorable (80% contribution) and unfavorable (20% contribution) H-bond acceptor groups. This finding can account for the fact compound 111 ($pIC_{50} = 6.17$) showed less activity by the introduction of HBA groups $-NPh(CH_3)_2$.

4. Conclusion

This work provides insight into the design of improved HDAC small molecule inhibitors for cancer treatment. The computer-aided drug design is known to have a wide range of applications in drug design and discovery, for example, QSAR analysis supplies a promising strategy to explore novel and better HDAC inhibitors. The selected 71 HDAC inhibitors from the reported literature were used for the 3D-QSAR study. The statistical quality of the generated model is demonstrated by internal and external cross-validations. The statistical parameters from 3D-QSAR models reveal that the results are reliable and significant with strong predictive ability. Furthermore, the CoMFA and CoMSIA contour maps reveal that steric, electrostatic, hydrophobic, and H-bond donor fields play a crucial part in the model. The findings demonstrate that our theoretical model results may contribute to the design of novel

HDAC small molecule inhibitors with enhanced activity for the treatment of cancer.

Consent for Publication

Not applicable.

Availability of Data and Materials

The data supporting the findings of this study are available within the article.

Funding

None.

Conflict of Interest

The authors declare no conflict of interest, financial or otherwise.

Acknowledgements

Declared none.

References

1. Tanabe, M., Fujiyama, S., & Horimoto, Y. (2016). Developmentally regulated GTP binding protein 2 (DRG2) and Nup107 are associated with epigenetic regulation via H2A. Z on promoter regions of specific genes in MCF7 breast

- cancer cells. *J Clin Epigenet*, 2, 4. 21-29.
2. Geng, H., Chen, H., Wang, H., & Wang, L. (2021). The histone modifications of neuronal plasticity. *Neural Plasticity*, 2021, 1-7.
 3. Aboyeji, C. M., Dunsin, O., Adekiya, A. O., Suleiman, K. O., Chinedum, C., Okunlola, F. O., ... & Owolabi, I. O. (2020). Synergistic and antagonistic effects of soil applied P and Zn fertilizers on the performance, minerals and heavy metal composition of groundnut. *Open Agriculture*, 5(1), 1-9.
 4. Banerjee, S., Adhikari, N., Amin, S. A., & Jha, T. (2019). Histone deacetylase 8 (HDAC8) and its inhibitors with selectivity to other isoforms: An overview. *European Journal of Medicinal Chemistry*, 164, 214-240.
 5. Yoon, J., Kim, S. J., An, S., Cho, S., Leitner, A., Jung, T., ... & Song, J. J. (2018). Integrative structural investigation on the architecture of human importin4_Histone H3/H4_Asfla complex and its histone H3 tail binding. *Journal of molecular biology*, 430(6), 822-841.
 6. Garmpis, N., Damaskos, C., Garmpi, A., Valsami, S., & Dimitroulis, D. (2019). Pharmacoeugenetics of Histone Deacetylase Inhibitors in Cancer. In *Pharmacoeugenetics* (pp. 501-521). Academic Press.
 7. Galvin, H. D., & Husain, M. (2019). Influenza A virus-induced host caspase and viral PA-X antagonize the antiviral host factor, histone deacetylase 4. *Journal of Biological Chemistry*, 294(52), 20207-20221.
 8. Asfaha, Y., Schrenk, C., Avelar, L. A. A., Hamacher, A., Pflieger, M., Kassack, M. U., & Kurz, T. (2019). Recent advances in class IIa histone deacetylases research. *Bioorganic & Medicinal Chemistry*, 27(22), 115087.
 9. Peng, X., Sun, Z., Kuang, P., & Chen, J. (2020). Recent progress on HDAC inhibitors with dual targeting capabilities for cancer treatment. *European Journal of Medicinal Chemistry*, 208, 112831.
 10. Hassell, K. N. (2019). Histone deacetylases and their inhibitors in cancer epigenetics. *Diseases*, 7(4), 57-70.
 11. Verza, F. A., Das, U., Fachin, A. L., Dimmock, J. R., & Marins, M. (2020). Roles of histone deacetylases and inhibitors in anticancer therapy. *Cancers*, 12(6), 1664-1692.
 12. Zhang, N., Sun, P., Jin, H., Yang, Y., Zhao, Q., Zhou, L., ... & Lu, L. (2020). Chidamide combined with paclitaxel effectively reverses the expression of histone deacetylase in lung cancer. *Anti-Cancer Drugs*, 31(7), 1-8.
 13. Agustriawan, D., Mulyono, H., Parikesit, A. A., & Nurdiansyah, R. (2019, June). Identification of Epigenetic Regulation on The Expression of The Aberrant Gene of Kidney Renal Clear Cell Carcinoma Patients Observed in a Specific Race. In *IOP Conference Series: Materials Science and Engineering* (Vol. 546, No. 6, p. 062001). IOP Publishing.
 14. Uesato, S., Hirata, Y., & Sasaki, T. (2017). Potential Application of 5-Aryl-Substituted 2-Aminobenzamide Type of HDAC1/2-Selective Inhibitors to Pharmaceuticals. *Current Pharmaceutical Design*, 23(40), 6149-6159.
 15. Kee, H. J., Sohn, I. S., Nam, K. I., Park, J. E., Qian, Y. R., Yin, Z., ... & Kook, H. (2006). Inhibition of histone deacetylation blocks cardiac hypertrophy induced by angiotensin II infusion and aortic banding. *Circulation*, 113(1), 51-59.
 16. Zhou, H., Li, Y., Li, J. (2020). 3D-QSAR Analysis of Naphthyltriazole (Lesinurad) Analogs as Potent Inhibitors of Urate Transporter 1. *Chinese Journal of Structural Chemistry*, 39(3), 421-436.
 17. Modi, S. J., & Kulkarni, V. M. (2018). 3D-QSAR analysis of pyrimidine derivatives as AXL kinase inhibitors as anticancer agents. *Journal of Applied Pharmaceutical Science*, 8(11), 015-027.
 18. Pandit, A., Yadav, K., Reddy, R. B., Sengupta, S., Sharma, R., & Chelvam, V. (2021). Structure activity relationships (SAR) study to design and synthesize new tubulin inhibitors with enhanced anti-tubulin activity: In silico and in vitro analysis. *Journal of Molecular Structure*, 1223, 129204.
 19. Li, X. Y. (2016). Design, Synthesis and Anti-Cancer Activity Evaluation of Small Molecular Inhibitors Based on Histone Deacetylases. PhD Thesis, Shan Dong University: Shan Dong.
 20. Dowlati Beirami, A., Hajimahdi, Z., & Zarghi, A. (2019). Docking-based 3D-QSAR (CoMFA, CoMFA-RG, CoMSIA) study on hydroquinoline and thiazinan-4-one derivatives as selective COX-2 inhibitors. *Journal of Biomolecular Structure and Dynamics*, 37(11), 2999-3006.
 21. Kasmi, R., Elmchichi, L., El Aissouq, A., Bouachrine, M., & Ouammou, A. (2021). In silico drug design: development of new pyrimidine-based benzothiazole derivatives, selective for CDK2. *Letters in Drug Design & Discovery*, 18(10), 961-975.
 22. Tong, J. B., Luo, D., Feng, Y., Bian, S., Zhang, X., & Wang, T. H. (2021). Structural modification of 4, 5-dihydro-[1, 2, 4] triazolo [4, 3-f] pteridine derivatives as BRD4 inhibitors using 2D/3D-QSAR and molecular docking analysis. *Molecular Diversity*, 25, 1855-1872.
 23. Wang, F., Yang, W., Shi, Y., & Le, G. (2015). Structural analysis of selective agonists of thyroid hormone receptor β using 3D-QSAR and molecular docking. *Journal of the Taiwan Institute of Chemical Engineers*, 49, 1-18.
 24. Jisha, R. S., Aswathy, L., Masand, V. H., Gajbhiye, J. M., & Shibi, I. G. (2017). Exploration of 3, 6-dihydroimidazo (4, 5-d) pyrrolo (2, 3-b) pyridin-2 (1H)-one derivatives as JAK inhibitors using various in silico techniques. In *Silico Pharmacology*, 5, 1-23.
 25. Abedi, H., Ebrahimzadeh, H., & Ghasemi, J. B. (2013). 3D-QSAR, CoMFA, and CoMSIA of new phenylloxazolidinones derivatives as potent HIV-1 protease inhibitors. *Structural Chemistry*, 24, 433-444.
 26. Sharma, M. C., Jain, S., & Sharma, R. (2017). In silico screening for identification of pyrrolidine derivatives dipeptidyl peptidase-IV inhibitors using COMFA, CoMSIA, HQSAR and docking studies. In *Silico Pharmacology*, 5, 1-12.
 27. Liu, H. C., Tang, S. Z., Lu, S., Ran, T., Wang, J., Zhang, Y. M., ... & Chen, Y. D. (2015). Studies on [5, 6]-fused bicyclic scaffolds derivatives as potent dual B-RafV600E/KDR inhibitors using docking and 3D-QSAR approaches. *International Journal of Molecular Sciences*, 16(10), 24451-24474.

-
28. Teixeira, C., Serradji, N., Maurel, F., & Barbault, F. (2009). Docking and 3D-QSAR studies of BMS-806 analogs as HIV-1 gp120 entry inhibitors. *European journal of medicinal chemistry*, 44(9), 3524-3532.
29. Patel, B., Patel, A., Patel, A., & Bhatt, H. (2020). CoMFA, CoMSIA, molecular docking and MOLCAD studies of pyrimidinone derivatives to design novel and selective tankyrase inhibitors. *Journal of Molecular Structure*, 1221, 128783.

Copyright: ©2023 Yuehong Huo, et al. This is an open-access article distributed under the terms of the Creative Commons Attribution License, which permits unrestricted use, distribution, and reproduction in any medium, provided the original author and source are credited.